

---

**This is an electronic reprint of the original article.  
This reprint *may differ* from the original in pagination and typographic detail.**

**Author(s):** Jordan, D.; Algora, Alejandro; Taín, J.L.; Rubio, B.; Agramunt, J.; Perez-Cerdan, A.B.; Molina, F.; Caballero, L.; Nácher, E.; Krasznahorkay, A.; Hunyadi, M.D.; Gulyás, J.; Vitéz, A.; Csatlós, M.; Csige, L.; Äystö, Juha; Penttilä, Heikki; Moore, Iain; Eronen, Tommi; Jokinen, Ari; Nieminen, Arto; Hakala, Jani; Karvonen, Pasi; Kankainen, Anu; Saastamoinen, Antti; Rissanen, Juho; Kessler, Thomas; Weber, Christine; Ronkainen, Jarmo; Bohannon, Seidun; Flores, Vilki; Veikko; Hepp; Ulrika; Riitta; Antti; Sami

**Title:** Total absorption study of the  $\beta$  decay of  $^{102,104,105}\text{Tc}$

**Year:** 2013

**Version:**

**Please cite the original version:**

Jordan, D., Algora, A., Taín, J.L., Rubio, B., Agramunt, J., Perez-Cerdan, A.B., Molina, F., Caballero, L., Nácher, E., Krasznahorkay, A., Hunyadi, M.D., Gulyás, J., Vitéz, A., Csatlós, M., Csige, L., Äystö, J., Penttilä, H., Moore, I., Eronen, T., . . . Faessler, A. (2013). Total absorption study of the  $\beta$  decay of  $^{102,104,105}\text{Tc}$ . *Physical Review C*, 87(4), Article 044318. <https://doi.org/10.1103/PhysRevC.87.044318>

All material supplied via JYX is protected by copyright and other intellectual property rights, and duplication or sale of all or part of any of the repository collections is not permitted, except that material may be duplicated by you for your research use or educational purposes in electronic or print form. You must obtain permission for any other use. Electronic or print copies may not be offered, whether for sale or otherwise to anyone who is not an authorised user.

**Total absorption study of the  $\beta$  decay of  $^{102,104,105}\text{Tc}$** 

D. Jordan,<sup>1</sup> A. Algora,<sup>1,2,\*</sup> J. L. Taín,<sup>1</sup> B. Rubio,<sup>1</sup> J. Agramunt,<sup>1</sup> A. B. Perez-Cerdan,<sup>1</sup> F. Molina,<sup>1</sup> L. Caballero,<sup>1</sup> E. Nácher,<sup>3</sup> A. Krasznahorkay,<sup>2</sup> M. D. Hunyadi,<sup>2</sup> J. Gulyás,<sup>2</sup> A. Vitéz,<sup>2</sup> M. Csatlós,<sup>2</sup> L. Csige,<sup>2</sup> J. Äystö,<sup>4</sup> H. Penttilä,<sup>4</sup> I. D. Moore,<sup>4</sup> T. Eronen,<sup>4</sup> A. Jokinen,<sup>4</sup> A. Nieminen,<sup>4</sup> J. Hakala,<sup>4</sup> P. Karvonen,<sup>4</sup> A. Kankainen,<sup>4</sup> A. Saastamoinen,<sup>4</sup> J. Rissanen,<sup>4</sup> T. Kessler,<sup>4</sup> C. Weber,<sup>4</sup> J. Ronkainen,<sup>4</sup> S. Rahaman,<sup>4</sup> V. Elomaa,<sup>4</sup> U. Hager,<sup>5</sup> S. Rinta-Antila,<sup>6</sup> T. Sonoda,<sup>7</sup> K. Burkard,<sup>8</sup> W. Hüller,<sup>8</sup> L. Batist,<sup>9</sup> W. Gelletly,<sup>10</sup> A. L. Nichols,<sup>10</sup> T. Yoshida,<sup>11</sup> A. A. Sonzogni,<sup>12</sup> K. Peräjärvi,<sup>13</sup> A. Petrovici,<sup>14,15</sup> K. W. Schmid,<sup>15</sup> and A. Faessler<sup>15</sup>

<sup>1</sup>*IFIC (CSIC-Univ. Valencia), Valencia, Spain*

<sup>2</sup>*Institute of Nuclear Research, Debrecen, Hungary*

<sup>3</sup>*IEM, CSIC, Madrid, Spain*

<sup>4</sup>*University of Jyväskylä, Jyväskylä, Finland*

<sup>5</sup>*TRIUMF, Vancouver, British Columbia, Canada*

<sup>6</sup>*Oliver Lodge Laboratory, University of Liverpool, United Kingdom*

<sup>7</sup>*RIKEN, 2-1 Hirosawa Wako Saitama, Japan*

<sup>8</sup>*GSI, Darmstadt, Germany*

<sup>9</sup>*PNPI, Gatchina, Russia*

<sup>10</sup>*University of Surrey, Guildford, United Kingdom*

<sup>11</sup>*Tokyo Institute of Technology, Japan*

<sup>12</sup>*NNDC, Brookhaven National Laboratory, New York, USA*

<sup>13</sup>*STUK, Helsinki, Finland*

<sup>14</sup>*National Institute for Physics and Nuclear Engineering, Bucharest, Romania*

<sup>15</sup>*Institut für Theoretische Physik, Universität Tübingen, Germany*

(Received 23 October 2012; revised manuscript received 18 February 2013; published 11 April 2013)

The  $\beta$ -feeding probabilities for three important contributors to the decay heat in nuclear reactors, namely  $^{102,104,105}\text{Tc}$ , have been measured using the total absorption spectroscopy technique. For the measurements, sources of very high isobaric purity have been obtained using a Penning trap (JYFLTRAP). A detailed description of the data analysis is given and the results are compared with high-resolution measurements and theoretical calculations.

DOI: [10.1103/PhysRevC.87.044318](https://doi.org/10.1103/PhysRevC.87.044318)

PACS number(s): 23.40.-s, 27.60.+j, 28.41.Fr, 29.30.Kv

**I. INTRODUCTION**

$\beta$ -strength or the related  $\beta$ -feeding distribution measurements are not only relevant to nuclear structure, but are of high interest in several practical applications, in particular nuclear technology.  $\beta$  decay is responsible for about 6%–8% of the energy released in a nuclear reactor during normal operation and for essentially most of the energy after shutdown. The so-called *decay heat* [1] depends on the design of the nuclear power plant and decreases as a function of time after shutdown. Independently of the type of reactor system one may consider, there are a number of important design and operating criteria which require an accurate knowledge of the heat generation. This may apply to the entire reactor or to an individual fuel element, and for times ranging from a few seconds to hundreds of days, and possibly years, following shutdown of the reactor. Failure to remove decay heat may cause the reactor core to heat up, resulting in possible core meltdown with dramatic consequences. Decay heat can be determined theoretically from known nuclear data, with computations based on the inventory of nuclei created during the fission process and after reactor shutdown, and their radioactive decay properties.

The decay-heat summation calculation method consists of summing up the activities of all fission product nuclides weighted with the mean  $\beta$ - and  $\gamma$ -ray energies released per disintegration:

$$\mathbf{f}(t) = \sum_i (\bar{E}_{\beta,i} + \bar{E}_{\gamma,i}) \lambda_i \mathbf{N}_i(t), \quad (1)$$

where  $\mathbf{f}(t)$  is the power function,  $\bar{E}_i$  is the mean decay energy of the  $i$  nuclide ( $\beta$  and  $\gamma$  components),  $\lambda_i$  is the decay constant of the  $i$ th nuclide, and  $\mathbf{N}_i(t)$  is the number of nuclides of type  $i$  at the cooling time  $t$  (for simplicity the  $\alpha$  decays of minor actinides are not included here). These calculations require extensive libraries of cross sections, fission yields, and decay data. However, depending on the case, the accuracy of the presently available decay data is not sufficient. This translates into larger uncertainties in the decay heat as a function of time and hence into higher safety margins implying larger economic costs.

The compiled decay data available in the international databases are typically the result of the evaluation of different measurements, using different techniques, but until recently they were mainly based on the use of Ge detectors. As a result, the decay data for a specific isotope can suffer from systematic uncertainties. One common problem is the existence of data that suffer from the *pandemonium effect*. This effect, first

\* [algora@ific.uv.es](mailto:algora@ific.uv.es)

pointed out by Hardy and coworkers [2], is related to the difficulties we face when constructing a nuclear level scheme in a  $\beta$ -decay study which relies on high-resolution detectors. In a high-resolution experiment the feeding probability to a certain level is deduced from the  $\gamma$  intensity balance of the  $\gamma$  rays feeding and de-exciting the level. If the  $\beta$  decay has a large  $Q_\beta$  value,  $\beta$  feeding at high excitation energies in the daughter can occur typically into a region of high-level density. As a consequence, the feeding probability can be very fragmented, which means that there may be many weak decay paths from the high-lying levels to the low-lying ones. The decay from the high-lying levels may also proceed by the emission of high-energy  $\gamma$  rays. If we fail to detect  $\gamma$  rays from these high-lying levels with Ge detectors, the resulting level scheme is incomplete and, in particular, the  $\beta$  feeding is incorrectly assigned to levels at low energy. The omission of nuclear levels fed in  $\beta$  decay has serious consequences for decay heat calculations: in such cases the total  $\gamma$  energy released in the decay process is underestimated and the total  $\beta$  energy is overestimated. The only way to avoid this problem is the application of the total-absorption technique to  $\beta$ -decay studies. In contrast to the high-resolution technique, the total-absorption technique is based on the detection of the  $\gamma$  cascades that follow the  $\beta$  decay. With the use of a highly efficient device, in essence a calorimeter placed around the source, an almost 100% efficiency for detecting  $\gamma$  cascades can be achieved and then the pandemonium effect can be avoided.

Despite the fact that in recent years improvements in the accuracy of the data in the world's major data libraries for decay-heat summation calculations have led to a fairly good description of the integral-type measurements for different fissioning nuclei, a discrepancy between the calculated and the measured electromagnetic component of the decay heat was detected in some particular cases [3]. This effect was carefully studied by the authors of Ref. [3] who called it *the  $\gamma$ -ray discrepancy*. The  $\gamma$ -ray discrepancy was noticed over cooling times that range from 300 to 3000 s after an instantaneous fission event in  $^{233,235,238}\text{U}$  and  $^{239}\text{Pu}$ , independently of the database used [JEF2.2, JNDC-V2 (actually JENDL), ENDF/B-IV]. For this reason the identification of the causes of the discrepancy was considered an important task by Yoshida and coworkers at that time. The discrepancy extended over a much longer cooling-time interval for the JEFF database (4–3000 s). The larger discrepancy is related to the philosophy underlying JEFF; namely, that only experimental values are used when available and they are not augmented by theoretical estimations even though they may be incomplete. The most plausible explanation of the discrepancy given in Ref. [3] is the underestimation of the total  $\gamma$  energy released in the decay of some nuclides that have a half-life of about 1000 s or that have a shorter half-life, but have a precursor with a half-life of about 1000 s in the  $\beta$ -decay chain. The work of Ref. [3] triggered our interest in the topic and experts in the field were contacted for additional cases of interest. The result was a priority list that contains nuclei that are large contributors to the decay heat and also to the inconsistencies in the different decay-data libraries used for the decay-heat summation calculations [4].

This work presents the results of the total-absorption measurements of the  $\beta$  decay of several isotopes with the

highest priority in the list ( $^{102,104,105}\text{Tc}$ ) and their impact in the decay-heat calculations. This article gives a more detailed description of the analysis than the previous letter [5] and provides additional experimental information. The article is structured as follows: in Sec. II, the experimental setup is described. In Sec. III a summary of the analysis technique used for total-absorption spectroscopy measurements and a detailed description of the different analyses performed for each nuclide studied is reported. The results are presented and discussed in Sec. IV. A comparison with the available decay-heat data from the different databases is also included in this section. Apart from addressing the decay-heat impact of these nuclei, our study is also important for nuclear structure. We will compare the deduced strength with calculations using the gross theory of beta decay and the *complex* excited variation after mean-field projection in realistic model spaces (VAMPIR) model. Gross theory has been used in the past as a substitute for experimental data that might suffer from the pandemonium effect [3]. The excited VAMPIR calculations represent the first effort to address nuclear aspects of these decays, which occur in a region where shape effects and shape coexistence might play an important role [6]. These calculations are presented in Sec. V for the nuclei  $^{102,104}\text{Tc}$ . The final conclusions are given in Sec. VI.

## II. EXPERIMENT

Technetium is a refractory element which is difficult to extract from conventional ion sources. Therefore, the experiments were performed at the Ion-Guide Isotope Separator On-Line (IGISOL) [7] facility of the University of Jyväskylä. In this facility nuclear reaction products recoiling out of a target are stopped in a gas (usually helium) and are transported by a gas flow through a differential pumping system directly into the acceleration stage of a mass separator. This process can be fast enough for some reaction products to survive as singly charged ions. The system is chemically insensitive which allows the extraction of refractory elements. The work presented here was an extension of a previous experiment where the  $\beta$  decays of  $^{104,105}\text{Tc}$  isotopes were measured. It involved combining a total-absorption spectrometer with the Penning trap at IGISOL (JYFLTRAP) [8] to measure the  $\beta$  decay of  $^{101}\text{Nb}$ ,  $^{102,104,105,106,107}\text{Tc}$ , and  $^{105}\text{Mo}$  [5]. The use of the Penning trap as a high-resolution isobaric separator allowed us to obtain very-high-purity sources which is of great importance in this kind of experiment.

To produce the isotopes of interest proton beams of 30 MeV and 50 MeV were delivered by the K-130 cyclotron at the University of Jyväskylä in order to induce fission in a natural U target of 15 mg/cm<sup>2</sup> thickness. Typical primary beam currents were about 4  $\mu\text{A}$ . The mass-separated activity produced by the IGISOL facility was further purified using JYFLTRAP. Following purification, the activity was carried to the Total-Absorption Gamma Spectrometer (TAGS) by a tape transport system using symmetric implantation and measurement cycles (see Table I for details). The TAGS was designed at the Nuclear Institute of St. Petersburg and consists of two NaI(Tl) cylindrical crystals (the larger crystal has dimensions

TABLE I. Relevant experimental data for the analyzed isotopes. The abbreviation “g.s.” stands for ground state.

Isotope	$T_{1/2}$ [s]	Cycle [s]	$Q_\beta$ [keV]	$S_n$ [keV]	$J^\pi$ (parent g.s.)	$J^\pi$ (daughter g.s.)	Ref.
$^{102}\text{Tc}$	5.28 (15)	1080	4532 (9)	9219.64 (5)	$1^+$	$0^+$	NDS 1998
$^{104}\text{Tc}$	1098 (18)	1800	5516 (6)	8901 (3)	$(3^+)$	$0^+$	NDS 2007
$^{105}\text{Tc}$	456 (6)	720	3746 (6)	5910.10 (11)	$(3/2^-)$	$3/2^+$	NDS 2005

$\varnothing = 200 \text{ mm} \times l = 200 \text{ mm}$  and has a longitudinal hole along its axis of  $\varnothing = 43 \text{ mm}$ ; the smaller crystal has dimensions  $\varnothing = 200 \text{ mm} \times l = 100 \text{ mm}$ ). The crystals were separated by 0.5 cm. Due to the different geometry of the crystals a Monte Carlo (MC) simulation was performed to determine the measurement position of highest efficiency [9]. This setup has an estimated total gamma efficiency of 70% at 5 MeV (see Fig. 1). A silicon detector was placed at the measuring point, inside the TAGS. In the setup a Ge detector was also placed at the collection point to continuously monitor the purity of the sources.

### III. ANALYSIS OF THE DATA

The analysis of the total-absorption spectra requires the solution of the “inverse problem”  $\mathbf{d} = \mathbf{R}(B) \cdot \mathbf{f}$  where  $\mathbf{d}$  represents the measured data,  $\mathbf{R}$  is the response matrix of the detector, and  $\mathbf{f}$  is the feeding distribution we wish to determine. The response function  $\mathbf{R}$  depends on the detector and branching ratios  $B$  of the levels in the daughter nucleus and can only be calculated using MC techniques. The analysis of the data presented here was carried out using the methods of analysis established by the Valencia group [10–13]. The response function was determined by means of the GEANT4 code [14]. The quality of the MC simulations was tested and fine tuned by comparing the result of the simulations with measured spectra of  $^{22,24}\text{Na}$ ,  $^{60}\text{Co}$ , and  $^{137}\text{Cs}$  radioactive sources.

The first step in the analysis of the TAGS data is the identification of possible contaminants and distortions of the

measured spectra. A TAGS is a highly efficient summing device with modest resolution compared with a high-resolution setup composed of Ge detectors. Therefore, a clean, high-purity source is of paramount importance. The extremely good separation of the isobars obtained with JYLTRAP (see Fig. 2) solves only part of the problem, since during the measurements the daughter decay can also contaminate our spectra. The contribution of the daughter activity can be reduced in general by proper choice of collection and measuring cycles for the decay of interest but in some cases cannot be completely avoided. In those cases the contribution of the daughter activity has to be evaluated and subtracted. For that, separate measurements of the daughter activity were performed. The factors needed for the subtraction of this unwanted activity were obtained by solving the Bateman equations for the decay chain in each case.

Another possible source of contamination is the background in the measurements. During the measurements the background was measured every two hours for one hour. In principle the idea was to use coincidences with the Si detector to obtain the spectrum to be analyzed and thus to avoid the contribution of the background. However, since this type of analysis requires a very careful evaluation of the Si efficiency and during the experiment the precision of the positioning of the tape was not high enough for this purpose, the measured singles spectra were used for the analysis. This has the advantage that much higher statistics can be used in the analysis. On the other hand the Si-TAGS coincidence spectra can be used to evaluate the correctness of the background subtraction coefficients by comparing the coincidence spectra with the subtracted spectra. Pulse pileup also distorts the

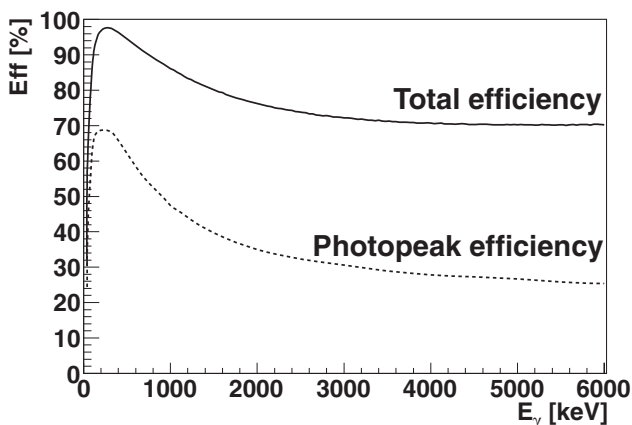


FIG. 1. Total and photopeak gamma detection efficiency of the TAGS setup (results of Monte Carlo simulations for monoenergetic gamma rays).

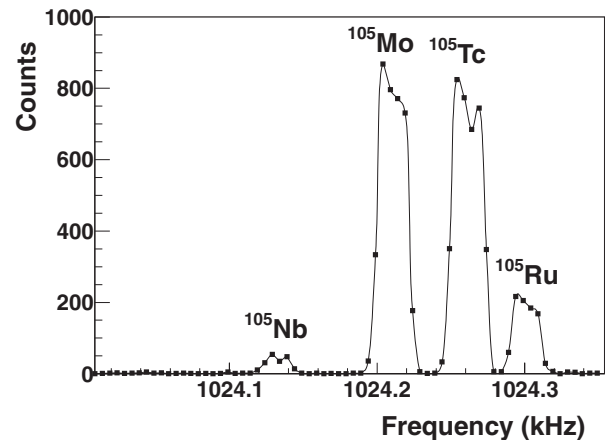


FIG. 2. Mass scan obtained with the Penning trap for  $A = 105$ . During the measurements the frequency in the trap is set for the isotope of interest.

TABLE II. Level density and  $\gamma$ -strength-function parameters used for the construction of the branching ratio matrix ( $B$ ) of the daughter nuclei (for details on the parametrizations, see Ref. [15]). The deformation parameters were taken from Ref. [17].

Isotope	Level-density parameters		Deformation parameter	$\gamma$ -strength function parameters								
	$a$	$\Delta$	$\beta$	$E1$			$M1$			$E2$		
				$E$ [MeV]	$\Gamma$ [MeV]	$\sigma$ [mb]	$E$ [MeV]	$\Gamma$ [MeV]	$\sigma$ [mb]	$E$ [MeV]	$\Gamma$ [MeV]	$\sigma$ [mb]
$^{102}\text{Ru}$	11.973	0.561	0.189	{ 14.391 17.291	{ 4.236 6.015	{ 270.7 190.6	8.788	4.0	6.643	13.504	4.886	2.323
$^{104}\text{Ru}$	12.0	0.56	0.253	{ 13.6711 17.722	{ 3.8402 6.304	{ 303.0 184.5	8.731	4.0	6.79	13.417	4.861	2.290
$^{105}\text{Ru}$	12.557	-1.013	0.291	{ 13.488 17.813	{ 3.743 6.367	{ 313.1 184.1	8.704	4.0	1.114	13.375	4.85	2.274

spectra. The pileup distortion was calculated as described in Ref. [10].

The second step in the analysis is the determination of the branching ratio matrix of the daughter nucleus ( $B$ ). In general, the experimental knowledge of the level scheme is limited to low excitation energies. For that reason, the proposed level scheme for each nuclide was adopted up to a certain excitation energy in the corresponding daughter nucleus. This information as well as other necessary data were obtained from the latest available compilation (see Table I). From this excitation energy up to the  $Q_\beta$  value the statistical nuclear model is used. This model is based on level densities and  $E1$ ,  $M1$ , and  $E2$   $\gamma$ -strength functions to generate an average branching ratio matrix (see, for example, Ref. [12]). The parameters used for each isotope are summarized in Table II. The high-resolution information available for the known part of the level scheme can be incomplete and spins and/or parities of some levels can be undefined (in brackets). As a result, assumptions must be made, leading to different possible level schemes for each nuclide (and hence many possible analyses).

Once the level scheme and the branching ratio matrix are defined,  $\mathbf{R}(B)$  is constructed recursively from the individual  $\gamma$  and  $\beta$  responses calculated in the MC simulations, as explained in Ref. [11]. Only allowed transitions are considered in this work. The ground-state to ground-state feeding is more difficult to determine in the TAGS singles mode measurements. Due to the working principle of the TAGS, only the penetration of the betas in the crystal as well as the associated bremsstrahlung can produce a signal in the detector for ground-state to ground-state transitions. Since no  $\gamma$  transitions are involved, the sensitivity of the setup to this kind of transition is reduced.

The last step consists of solving the inverse problem to determine the  $\beta$ -feeding distribution. For this purpose, the expectation-maximization method applied to the TAGS problems [12,13] has been used. In the analysis we normally exclude the last 300–400 keV of the spectrum to avoid unphysical oscillations in the deduced feeding due to the lower statistics.

The  $\beta$ -feeding distribution, normalized to unity, is used to calculate the mean  $\gamma$  and  $\beta$  energies released in the decay

through the equations

$$\bar{\mathbf{E}}_\gamma = \sum_i \mathbf{E}_i \mathbf{I}_i, \quad (2)$$

$$\bar{\mathbf{E}}_\beta = \sum_i \langle \mathbf{E}_\beta \rangle_i \mathbf{I}_i, \quad (3)$$

where  $\mathbf{E}_i$  is the energy of the level  $i$ ,  $\mathbf{I}_i$  is the normalized feeding (or beta intensity) to level  $i$ , and  $\langle \mathbf{E}_\beta \rangle_i$  is the mean energy of the  $\beta$  continuum populating level  $i$  [with endpoint ( $Q_\beta - E_i$ )]. The mean beta energy was calculated assuming that the beta continuum has an allowed shape. The average energies have two associated kinds of error. The first one is related to the uncertainties in the feeding distribution and can be obtained using the equations

$$\sigma_{\bar{\mathbf{E}}_\gamma}^2 = \sum_i \mathbf{E}_i^2 \sigma_{\mathbf{I}_i}^2, \quad (4)$$

$$\sigma_{\bar{\mathbf{E}}_\beta}^2 = \sum_i \langle \mathbf{E}_\beta \rangle_i^2 \sigma_{\mathbf{I}_i}^2, \quad (5)$$

$$\sigma_{\mathbf{I}_i}^2 = \sum_k \frac{\sigma_{\mathbf{f}_k}^2}{(\sum_k \mathbf{f}_k)^2}, \quad (6)$$

corresponding to the errors in  $\gamma$  energy,  $\beta$  energy, and normalized  $\beta$  feeding to level  $i$ ,  $\sigma_{\mathbf{I}_i}$ , respectively. In the last equation  $\mathbf{f}_k$  is the feeding to level  $k$  (not normalized) and  $\sigma_{\mathbf{f}_k}$  is the corresponding error, deduced from the analysis. The second kind of error in the mean energies is the systematic error due to the strong dependence of the average energies on the assumptions made for the construction of the response matrix. This error is usually much larger than the error obtained from the  $\beta$ -feeding distribution [Eqs. (4) and (5)].

The normalized  $\beta$ -feeding distribution has also been used for the determination of the  $\beta$ -strength distribution  $S_\beta(E_x)$ .  $S_\beta(E_x)$  is commonly defined as an average quantity which represents the mean value of the total rate for all the transitions occurring to levels inside a certain energy bin  $\Delta E_x$  at the central excitation energy  $E_x$ . It is related to the normalized  $\beta$ -feeding distribution by

$$S_\beta(E_x) = \frac{1}{T_{1/2}} \sum_{E_x \in \Delta E_x} \frac{1}{\Delta E_x} \frac{I_\beta(E_x)}{f(Q_\beta - E_x)}, \quad (7)$$

where  $T_{1/2}$  is the  $\beta$ -decay half-life and  $f(Q_\beta - E_x)$  is the statistical rate Fermi function, which depends both on the  $\beta$  process type and on the energy available in the decay  $Q_\beta - E_x$ .

In the following subsections, the different analyses performed for the decay of each nucleus will be described in detail.

#### A. $^{104}\text{Tc} \rightarrow ^{104}\text{Ru}$ decay

The spin-parity of the ground state of  $^{104}\text{Tc}$  is reported tentatively (in brackets) in Ref. [16]. For the analysis  $J^\pi = 3^+$  was assumed. Bearing this in mind as well as the fact that only allowed Gamow-Teller transitions are considered, the ground state of  $^{104}\text{Ru}$  should not be directly populated in the decay, which is in agreement with high-resolution measurements. The  $^{104}\text{Tc}$  decay has a large  $Q_\beta$  value, 5516 (6) keV. With such an energy window, the number of possible levels that can be populated in the decay is large. However, on the information available on the decay on this isotope the number of levels known to be populated is not so high (Ref. [16]). In general, the known levels from the high-resolution  $^{104}\text{Ru}$  level scheme at low excitation energy are well defined. There are two levels with spins and parities shown in brackets at 1974.8 keV, ( $6^-, 7$ ) and 1872 keV, ( $5^+$ ). In the construction of the branching ratio matrix a  $6^-$  was assumed for the level at 1974.8 keV and  $5^+$  for the 1872 keV level. In such a context, the analyses were performed assuming the known level scheme up to two excitation energies, 1515.4 and 2080.8 keV. For the former, two different excitation energies were considered for the starting energy of the unknown part of the level scheme, namely 1720 and 1840 keV. With the known level scheme up to 2080.8 keV, the statistical model was used from 2120 keV up to the  $Q$  value.

The results presented in this work correspond to the analysis assuming a known level scheme up to 1515.4 keV, and the statistical model from 1720 keV up to the  $Q$  value using the parameters given in Table II. This analysis has the advantage that all the uncertainties in the known level scheme are removed and it also has the lowest  $\chi^2$  (defined as the square of the difference between the analyzed spectrum and the reconstructed spectrum after the analysis [ $\mathbf{R}(B) \cdot \mathbf{f}^{\text{final}}$ ]). The reconstructed spectrum is compared with the experimental data in the upper panel of Fig. 3. Both spectra include the contaminants (background and pileup) which are also plotted in the figure in order to show their relative contributions. The fact that the experimental and reconstructed data are indistinguishable confirms the quality of the analysis. Figure 4 shows the comparison of the subtracted spectrum, free of contaminants with the results of the reconstructed spectrum.

In the lower panel of Fig. 3 the deduced TAGS  $\beta$ -feeding distribution is shown (dots) in comparison with the high-resolution  $\beta$ -feeding distribution (solid gray line). Several differences can be seen. The TAGS result assigns less  $\beta$ -feeding than the high-resolution results to excitation energies below the last known level considered (1515.4 keV). Above this energy level, the TAGS  $\beta$  feeding is distributed among many levels up to the  $Q$  value (5516 keV) in contrast with the high-resolution  $\beta$  feeding where the last populated energy level is at 4267.7 keV excitation. In brief, the  $\beta$ -feeding distribution is shifted to higher excitation energies in the daughter nucleus

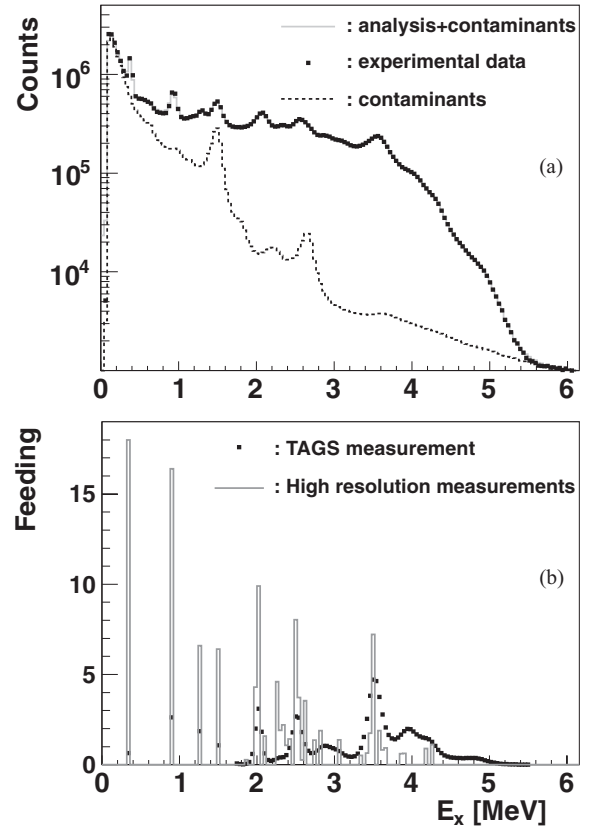


FIG. 3. (a) Comparison of reconstructed spectrum after analysis with experimental data, including the contaminants, for  $^{104}\text{Tc}$ . The contribution of the contaminants is also presented. (b) Comparison of the  $\beta$ -feeding distribution with that derived from the high-resolution measurements (Ref. [16]).

as expected for nuclei where the high-resolution data suffer from the pandemonium effect. Despite the differences, the structure formed by the TAGS feeding distribution has peaks at the same energies as the levels detected in high-resolution measurements (2, 2.5, and 3.5 MeV). The deduced feeding distribution is given in Table IV.

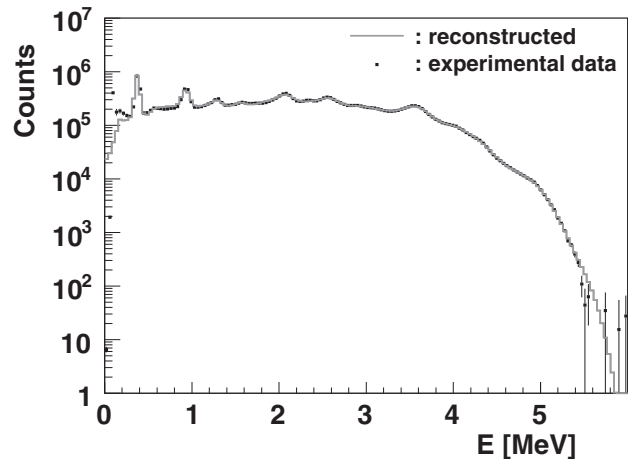


FIG. 4. Comparison of reconstructed spectrum after analysis with experimental subtracted data, free of contaminants, for  $^{104}\text{Tc}$ .

**B.  $^{105}\text{Tc} \rightarrow ^{105}\text{Ru}$  decay**

The decay of  $^{105}\text{Tc}$  has the smallest  $Q_\beta$  value of the nuclei presented here, 3746 keV, but at the same time, it has the highest number of levels predicted by calculations based on the statistical model. As in the  $^{104}\text{Tc}$  case, the spin and parity of the parent ground state is tentatively given in brackets as  $(3/2^-)$ , and  $3/2^-$  was assumed. Thus, the ground-state to ground-state transition is a first-forbidden transition ( $3/2^- \rightarrow 3/2^+$ ). However, some feeding to the ground state of  $^{105}\text{Ru}$  was detected with high-resolution setups ( $<9\%$  according to Ref. [18]). For this particular case several analyses were performed varying the feeding to the ground state from zero feeding to 9% which was considered as an upper limit.

The known level scheme of  $^{105}\text{Ru}$  is incomplete having uncertainties in the spins and parities of several levels. In this case, the high-resolution level scheme was accepted up to the excitation energy 1325.5 keV. Because of the uncertainties in the level scheme, the number of possible level schemes is very large, and analyses for only some representative cases were performed. Two typical examples are presented in Table III. For the construction of the unknown part of both level schemes, the statistical model was applied in the usual way from 1360 keV up to the  $Q$  value. It is important to mention that, although different level schemes were used, the results obtained for each case are very similar. The results given in this work correspond to the analysis using level scheme 2 (the one with the smallest  $\chi^2$ ) and fixing the feeding to the ground state to 9%. This upper limit could be consistent with the high-resolution measurements. However, for completeness, the values obtained fixing the feeding to the  $^{105}\text{Ru}$  ground state to be zero are also given in Table IV and were also used in the next section to calculate the mean energies.

In the lower panel of Fig. 5, the feeding distribution deduced for the decay of  $^{105}\text{Tc}$  is presented. As in the extraction of the feeding for  $^{104}\text{Tc}$  and despite the lower  $Q$  value for the decay,

TABLE III. Two representative level schemes used in the analysis. Only the levels with uncertain spins and parities are included in this table.

$E_{\text{lev}}$ [keV]	Adopted NDS	Level scheme 1	Level scheme 2
163.8	$3/2^+, 5/2^+$	$3/2^+$	$5/2^+$
246.4	$(5/2^-, 3/2)$	$5/2^-$	$3/2^-$
272.7	$(3/2, 5/2^+)$	$3/2^+$	$5/2^+$
441.9	$3/2^+, 5/2^+$	$3/2^+$	$5/2^+$
578.1	$(5/2^+, 3/2)$	$5/2^+$	$3/2^+$
582.1	$3/2^+, 5/2^+$	$3/2^+$	$5/2^+$
644	$(5/2, 3/2)$	$5/2^-$	$3/2^-$
725.9	$(5/2^-, 7/2, 9/2^+)$	$7/2^+$	$5/2^-$
756.7	$3/2^+, 5/2^+$	$3/2^+$	$5/2^+$
824.3	$3/2^+, 5/2^+$	$3/2^+$	$5/2^+$
841.1	$7/2^+, 9/2^+$	$7/2^+$	$9/2^+$
956.7	$(3/2, 5/2^+)$	$3/2^+$	$5/2^+$
967.1	$(1/2, 3/2, 5/2^+)$	$3/2^+$	$5/2^+$
1058.8	$(3/2^+, 5/2, 7/2^+)$	$5/2^+$	$7/2^+$
1180.1	$(3/2^+, 5/2^+)$	$5/2^+$	$3/2^+$
1325.5	$(1/2, 3/2)$	$3/2^+$	$1/2^+$

TABLE IV. Feeding distributions for  $^{104}\text{Tc}$ ,  $^{105}\text{Tc}$ , and  $^{102}\text{Tc}$  decays. The values are given for energy bins of 40 keV.

Energy (keV)	$^{104}\text{Tc}$ feeding [%]	$^{105}\text{Tc}$ feeding [%]	$^{105}\text{Tc}$ feeding [%]	$^{102}\text{Tc}$ feeding [%]
0	0	9.0	0	92.9
20	0	0	0	0
60	0	0	0	0
100	0	0	0	0
140	0	0	0	0
180	0	0	0	0
220	0	0	0	0
260	0	0.5103	0.7308	0
300	0	0	0	0
340	0.6485	5.1187	5.7255	0
380	0	0	0	0
420	0	0	0	0
460	0	0	0	2.0453
500	0	0.5775	0.6726	0
540	0	0	0	0
580	0	0	0	0
620	0	0	0	0
660	0	0.9339	1.0295	0
700	0	0	0	0
740	0	1.7171	1.9515	0
780	0	4.3247	4.6953	0
820	0	0	0	0
860	0	0	0	0
900	2.6201	0	0	0
940	0	0	0	0.5833
980	0	0	0	0
1020	0	0	0	0
1060	0	0	0	0
1100	0	0	0	0.3990
1140	0	0	0	0
1180	0	0	0	0
1220	0	0	0	0
1260	1.8527	0	0	0
1300	0	0	0	0
1340	0	0	0	0
1380	0	0.8642	0.9596	0
1420	0	0.4742	0.5263	0
1460	0	0.3064	0.3401	0
1500	1.0752	0.2216	0.2455	0
1540	0	0.1685	0.1861	0
1580	0	0.1491	0.1643	1.4352
1620	0	0.1694	0.1863	0
1660	0	0.2486	0.2729	0
1700	0	0.4730	0.5187	0
1740	0.0625	1.2078	1.3233	0
1780	0.0298	3.5053	3.8378	0
1820	0.0273	6.8953	7.5466	0.4766
1860	0.0476	5.9110	6.4683	0
1900	0.1428	2.5773	2.8210	0
1940	0.5880	1.1285	1.2356	0
1980	2.0008	0.8251	0.9034	0.4774
2020	3.0986	0.9572	1.047	0.1561
2060	1.8260	1.4157	1.5496	0.0393
2100	0.6276	2.2524	2.4648	0.0153
2140	0.2637	3.1681	3.4671	0.0115

TABLE IV. (Continued).

Energy (keV)	$^{104}\text{Tc}$ feeding [%]	$^{105}\text{Tc}$ feeding [%]	$^{105}\text{Tc}$ feeding [%]	$^{102}\text{Tc}$ feeding [%]
2180	0.2085	3.4730	3.8007	0.0120
2220	0.2637	3.1258	3.4204	0.0139
2260	0.3620	2.8070	3.0717	0.0170
2300	0.4058	2.7775	3.0396	0.0208
2340	0.4237	2.8116	3.0768	0.0244
2380	0.5346	2.6939	2.9476	0.0281
2420	0.9317	2.4394	2.6694	0.0304
2460	1.7942	2.2587	2.4714	0.0313
2500	2.6709	2.1649	2.3689	0.0348
2540	2.5991	2.0856	2.2822	0.0423
2580	1.8065	1.9380	2.1206	0.0545
2620	1.1319	1.6839	1.8430	0.0730
2660	0.7681	1.4413	1.5771	0.0900
2700	0.6357	1.2760	1.3962	0.0979
2740	0.6576	1.2672	1.3864	0.1021
2780	0.7879	1.4357	1.5708	0.1145
2820	0.9558	1.7316	1.8946	0.1361
2860	1.0483	1.9363	2.1186	0.1454
2900	1.0395	1.7774	1.9447	0.1120
2940	0.9797	1.2824	1.4030	0.0567
2980	0.9198	0.7686	0.8409	0.0236
3020	0.8531	0.4363	0.4774	0.0120
3060	0.7522	0.2697	0.2951	0.0090
3100	0.6298	0.1958	0.2142	0.0100
3140	0.5185	0.1652	0.1808	0.0136
3180	0.4458	0.1493	0.1633	0.0186
3220	0.4276	0.1324	0.1448	0.0229
3260	0.4724	0.1086	0.1188	0.0243
3300	0.6131	0.0821	0.0898	0.0214
3340	0.9219	0.0586	0.0641	0.0155
3380	1.5288	0.0402	0.0440	0.0096
3420	2.5490	0.0268	0.0293	0.0056
3460	3.8181	0.0174	0.0191	0.0034
3500	4.7153	0.0113	0.0124	0.0024
3540	4.6348	0.0076	0.0084	0.0019
3580	3.7602	0.0057	0.0063	0.0017
3620	2.7798	0.0050	0.0054	0.0017
3660	2.0627	0.0050	0.0055	0.0016
3700	1.6419	0.0059	0.0065	0.0016
3740	1.4504			0.0015
3780	1.4162			0.0014
3820	1.4990			0.0014
3860	1.6674			0.0013
3900	1.8561			0.0013
3940	1.9819			0.0013
3980	1.9739			0.0012
4020	1.8423			0.0012
4060	1.6826			0.0011
4100	1.5621			0.0010
4140	1.5061			0.0010
4180	1.4783			0.0010
4220	1.4127			0.0010
4260	1.2586			0.0010
4300	1.0356			0.0011
4340	0.8119			0.0011
4380	0.6353			0.0012
4420	0.5175			0.0012

TABLE IV. (Continued).

Energy (keV)	$^{104}\text{Tc}$ feeding [%]	$^{105}\text{Tc}$ feeding [%]	$^{105}\text{Tc}$ feeding [%]	$^{102}\text{Tc}$ feeding [%]
4460	0.4463			0.0012
4500	0.4071			0.0012
4540	0.3842			
4580	0.3710			
4620	0.3634			
4660	0.3608			
4700	0.3636			
4740	0.3703			
4780	0.3747			
4820	0.3677			
4860	0.3426			
4900	0.2999			
4940	0.2478			
4980	0.1956			
5020	0.1494			
5060	0.1117			
5100	0.0819			
5140	0.0591			
5180	0.0423			
5220	0.0303			
5260	0.0218			
5300	0.0160			
5340	0.0121			
5380	0.0095			
5420	0.0079			
5460	0.0071			
5500	0.0068			

a shift in the feeding distribution to higher excitation energies in comparison with high-resolution measurements is observed.

### C. $^{102}\text{Tc} \rightarrow ^{102}\text{Ru}$ decay

In Fig. 6 part of the decay chain of mass 102 is shown.  $^{102}\text{Tc}$  represented the most challenging and complex case among the isotopes studied. The direct production of this isotope was low and difficulties were experienced in separating it from the parent  $^{102}\text{Mo}$  isotope even using the Penning trap (see Fig. 7). The only solution was to produce the  $^{102}\text{Tc}$  activity through the parent  $^{102}\text{Mo}$  which was produced with higher yield. It also ensured the population of the  $^{102}\text{Tc}$  ground state free from the isomeric state of  $^{102}\text{Tc}$  which decays to high spin levels in  $^{102}\text{Ru}$ . However, the difference between the half-lives of  $^{102}\text{Mo}$  (minutes) and  $^{102}\text{Tc}$  (seconds) made it impossible to measure the two decays separately. The parent activity therefore had to be subtracted subsequently as a contaminant in the analysis. The difference in the half-lives also introduces a self-consistency requirement: one expects that every decay of  $^{102}\text{Mo}$  will produce a decay of  $^{102}\text{Tc}$ . This requirement was imposed in the normalization factor used for the  $^{102}\text{Mo}$  decay contamination.

The level scheme of the  $^{102}\text{Ru}$  nucleus is quite well known experimentally (spins and parities) up to an excitation energy of 1873.2 keV. There is only one level with an uncertain

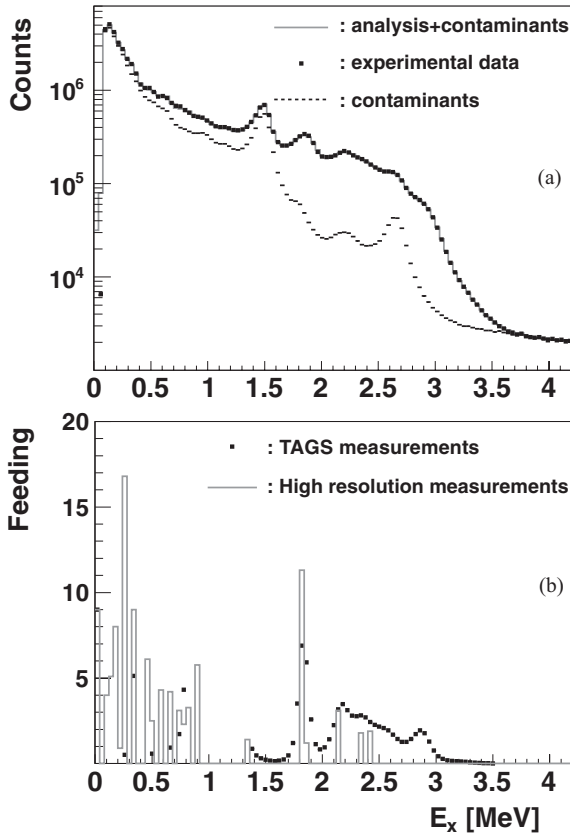


FIG. 5. (a) Comparison of reconstructed spectrum after analysis with experimental data for the decay of  $^{105}\text{Tc}$ . The contribution of the contaminants is also presented. (b)  $\beta$ -feeding distribution obtained from analysis compared with the one from high-resolution measurements.

spin-parity assignment at an excitation energy of 1602.9 keV ( $3,4^+$ ) but it is not fed directly in the decay. We assumed  $3^+$  for this level in the analysis. For the construction of the response matrix of the  $^{102}\text{Tc}$  decay the known level scheme up to 1873.2 keV was adopted and from 1960 keV up to the  $Q$  value the statistical nuclear model was applied. The decay of  $^{102}\text{Mo}$  has a relatively small  $Q_\beta$  value [ $Q_\beta = 1014$  (23) keV] which implies that this decay most probably does not suffer from the pandemonium effect and the information available in Ref. [19] can be considered to be reliable. To obtain a measure

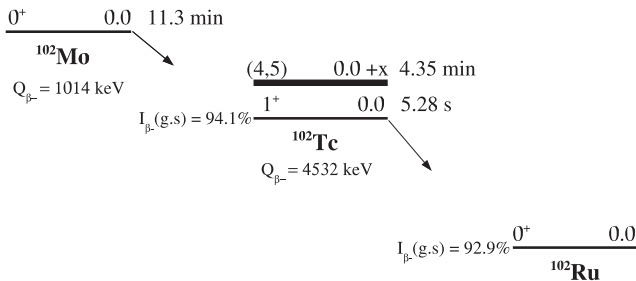


FIG. 6. Decay chain of mass 102 relevant to the present experiment.

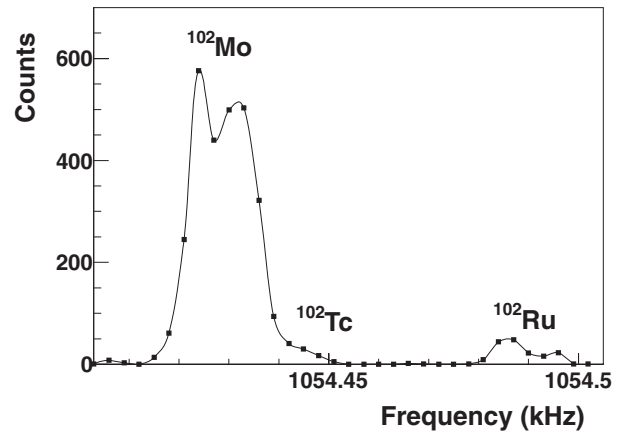


FIG. 7. Mass scan for  $A = 102$ .

of the contamination introduced by  $^{102}\text{Mo}$ , the decay of this nucleus has been simulated based on the information from Ref. [19] using the MC response functions calculated for the analysis.

Due to the contamination introduced by the decay of  $^{102}\text{Mo}$ , the analysis of the decay of  $^{102}\text{Tc}$  required considerations additional to the conventional TAGS analysis. The last level populated in the decay of  $^{102}\text{Mo}$  is at an excitation of 359.9 keV and the first-excited level populated in the decay of  $^{102}\text{Tc}$  is at an excitation energy of 475.0 keV. The energy difference between these two levels allowed us to determine self-consistently the normalization factor of the contamination of the decay of  $^{102}\text{Mo}$  in the measured spectra. The analysis was performed in two steps. In the first step, the analysis of the part of the measured TAGS spectra in which the contribution of the decay of  $^{102}\text{Tc}$  was dominant ( $E_x > 475$  keV) was performed. For this partial analysis a certain value for the ground-state feeding of the decay of  $^{102}\text{Tc}$  into  $^{102}\text{Ru}$  was assumed (the ground-state feeding of the beta decay of  $^{102}\text{Tc}$  into  $^{102}\text{Ru}$  is 92.9% according to Ref. [19]). The ground-state feeding of this decay was taken as a variable parameter. The total number of  $^{102}\text{Tc}$  decays can be obtained from the results of this first analysis. This number, because of the constraint on the half-lives, should be equal to the number of decays of  $^{102}\text{Mo}$ . Once the contribution of the decay of  $^{102}\text{Mo}$  to the measured spectrum has been obtained, the analysis is done in the conventional way, considering  $^{102}\text{Mo}$  as a contaminant and analyzing the full spectrum range for the decay of  $^{102}\text{Tc}$ . Additionally, different possible responses of the decay of  $^{102}\text{Mo}$  can also be considered, varying the ground-state feeding to  $^{102}\text{Tc}$ . Following this recipe several analyses were performed iteratively, varying accordingly the assumed ground-state feeding of  $^{102}\text{Tc}$  and  $^{102}\text{Mo}$  until the best fit to the experimental data was obtained. The suitability of the fit was studied through the evaluation of the  $\chi^2$ , defined as

$$\chi^2 = \sum \frac{[S_{\text{expt.}} - (^{102}\text{Mo} + ^{102}\text{Tc})]^2}{(^{102}\text{Mo} + ^{102}\text{Tc})^2}, \quad (8)$$

where  $S_{\text{expt.}}$  refers to the experimental spectrum and  $^{102}\text{Mo}$  and  $^{102}\text{Tc}$  are the  $^{102}\text{Mo}$  and  $^{102}\text{Tc}$  reconstructed decay spectra obtained from the analyses, respectively.

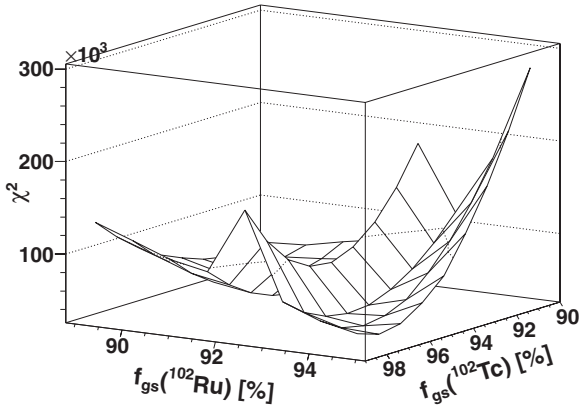


FIG. 8. Plot of the  $\chi^2$  values obtained using different  $^{102}\text{Tc}$  and  $^{102}\text{Ru}$  ground-state feedings [see Eq. (8) for the  $\chi^2$  definition].

The different decay response functions for the decay of  $^{102}\text{Mo}$  were constructed varying the ground-state feeding from 90% to 98% in steps of 1% (including the value in the literature, 94.1%). On the other hand, the  $^{102}\text{Ru}$  ground-state feeding was fixed to 89%, 90%, 91%, 91.5%, 92%, 92.5%, 92.9%, 94%, and 95%, respectively. A three-dimensional  $\chi^2$  plot was constructed (Fig. 8). The absolute minimum  $\chi^2$  corresponds to the case where there is 96% feeding to the  $^{102}\text{Tc}$  ground state and 94% feeding to the  $^{102}\text{Ru}$  ground state. The value of the  $\chi^2$  obtained using the feedings given in the nuclear data sheets (NDSs) is quite close to the minimum, this is the reason why the original experimental values (94.1% and 92.9%, respectively, for  $^{102}\text{Tc}$  and  $^{102}\text{Ru}$  ground-state feedings) were kept.

TAGS and high-resolution feeding distributions are shown in the lower panel of Fig. 9. Because the decay of this nucleus is dominated by the transition to the ground state, the feeding to this state has been divided by a factor of 20 in both cases in order to show better the feeding to excited states which are populated with lower probability. Although the feeding to the ground state in our analysis was fixed to the value given by high-resolution measurements, the feeding distributions differ slightly. A comparison of the results of the reconstructed spectrum (gray continuous line) from our analysis with the measured spectrum (black dots) is also given in the upper part of Fig. 9 which again shows excellent agreement. Both spectra include all the contaminants: background, pileup, and  $^{102}\text{Mo}$  decay. The contribution of those contaminants is also shown (dotted line) in this plot. As in the other cases, the deduced feeding distribution is given in Table IV.

#### IV. AVERAGE ENERGIES AND EFFECT ON DECAY-HEAT SUMMATION CALCULATIONS

The  $\gamma$  and  $\beta$  average energies from experimental TAGS data and ENDF/B-VII.0 [20] and JEFF-3.1 [21] databases are summarized in Table V and were already presented in Ref. [5]. In general, the average gamma energies have increased and the average beta energies have decreased in comparison with the values in the databases. The differences in the values of the average energies with respect to the database values

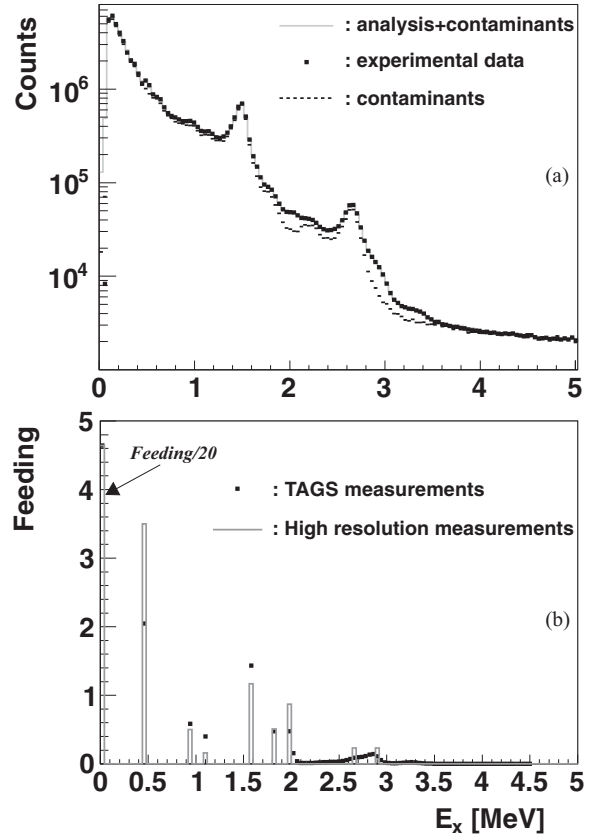


FIG. 9. (a) Comparison of reconstructed and experimental data including contaminants for the decay of  $^{102}\text{Tc}$ . The contribution of the contaminants is also presented (dotted line). (b)  $\beta$ -feeding distribution obtained from experiment compared with high-resolution measurements.

are a sign that the analyzed isotopes were suffering from the pandemonium effect. In the case of  $^{102}\text{Tc}$  decay, the differences are not as relevant as for the other two nuclei. This can be easily understood if we take into account how a total-absorption spectrometer works. With a TAGS we are able to detect the weak  $\gamma$  cascades coming from feeding at high excitation energies and, thus, determine the feeding at these energies. This is not always possible using high-resolution setups. However, the fact that most of the  $\beta$  feeding goes to the ground state of  $^{102}\text{Ru}$  means that only a few percent of the feeding will be distributed among levels at higher excitation. In such a situation, the pandemonium effect cannot be expected to be significant.

The adopted values for  $^{105}\text{Tc}$  have been obtained by fixing the feeding to the ground state to the upper limit 9%. If the ground-state feeding is fixed to zero, the values of the average energies differ slightly:  $\bar{E}_\beta = 683$  keV and  $\bar{E}_\gamma = 1999$  keV. The impact of the TAGS values is better seen if we include our average energies in the databases and plot the calculated decay heat for  $^{239}\text{Pu}$  [22]. The results are shown in Figs. 10 and 11. In both pictures, the color convention is the following: black squares correspond to experimental measurements (Tobias compilation [23], the standard compilation in the field) and the black and dotted lines represent the theoretical calculations

TABLE V. Results of the average  $\beta$  and  $\gamma$  energies and their comparison with databases. The difference is calculated with respect to the JEFF-3.1 database.

Nuclide	Energy type	TAGS experiment [keV]	JEFF-3.1 [keV]	ENDF/B-VII.0 [keV]	Difference [keV]
$^{102}\text{Tc}$	$\beta$	1935 (11)	1945 (16)	1945 (16)	-10
$^{102}\text{Tc}$	$\gamma$	106 (23)	81 (10)	81 (5)	25
$^{104}\text{Tc}$	$\beta$	931 (10)	1595 (75)	1595 (75)	-664
$^{104}\text{Tc}$	$\gamma$	3229 (24)	1890 (31)	1890 (31)	1339
$^{105}\text{Tc}$	$\beta$	764 (81)	1310 (173)	1310 (205)	-546
$^{105}\text{Tc}$	$\gamma$	1825 (174)	668 (19)	665 (19)	1157

using ENDF/B-VII with and without, respectively, our average energies.

Figure 10 shows the  $\gamma$  decay-heat component. The effect of our data is to pull up the dotted line close to the experimental points within the error bars in the 50–3000 s range, which is an improvement compared with the summation calculations based on the version of the database that does not include our values for the Tc isotopes. In particular, for the range from 300 to 3000 s, the increment in the summation calculations solves a large part of the  $\gamma$ -ray discrepancy. The  $\beta$  decay-heat component (Fig. 11) does not show a significant change. The effect of the average energies of the isotopes of interest in the database is to pull down the dotted line, but it remains inside the experimental error bars.

The impact of these results on summation calculations for  $^{235}\text{U}$  was also evaluated [22]. The  $\gamma$  and  $\beta$  decay-heat components were calculated for an instantaneous fission event in  $^{235}\text{U}$ . The effect of the inclusion of the TAGS data in the nuclear database is similar to the case of  $^{239}\text{Pu}$  but much less impressive as can be seen in Figs. 12 and 13. This is related to the cumulative fission yields. For  $^{239}\text{Pu}$ , the cumulative fission yields for the isotopes presented here is approximately 17.8% of the fission, while for  $^{235}\text{U}$  it is only 7.1%.

It is worth deducing the  $\beta$ -strength distributions from our TAGS data and comparing them with the  $\beta$ -strength distributions from high-resolution measurements. In the same plots, the calculated  $\beta$ -strength distributions using the gross theory

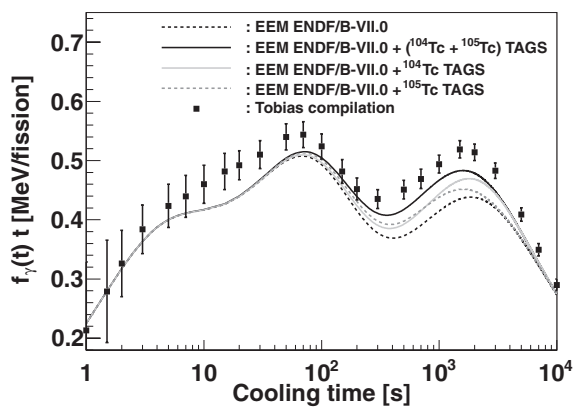


FIG. 10. Comparison of calculated  $\gamma$  decay-heat component with data of Tobias [23] after an instantaneous fission event in  $^{239}\text{Pu}$  without and with the inclusion of  $^{104}\text{Tc}$  and  $^{105}\text{Tc}$  TAGS measurements. The individual contributions of the  $^{104}\text{Tc}$  and  $^{105}\text{Tc}$  decays are also presented.

[24,25] are also shown. The gross theory of nuclear  $\beta$  decay is commonly used in databases for theoretical estimations of nuclei with incomplete experimental data. The comparison between TAGS, high-resolution, and gross theory strength distributions is presented for the decay of  $^{104}\text{Tc}$  in Fig. 14. The black dots correspond to the TAGS strength distribution, the gray line represents the strength from high-resolution measurements, and the black dotted line is the calculated  $\beta$ -strength distribution using gross theory. For convenience, the strength distributions have been multiplied by a factor of  $10^6$  and are represented on a logarithmic scale. The strength distribution from the high-resolution measurements extends up to 4268 keV excitation energy; the last populated level detected in high-resolution studies. In the TAGS measurements, above this energy, additional strength is found for levels in the region where no high-resolution feeding was found earlier.

The differences are seen better if the strength is summed up to the  $Q$  value for the three distributions and the accumulated strength is shown (Fig. 15). Up to the last known level in high resolution, the gross theory predicts an accumulated strength value one order-of-magnitude higher than the TAGS and high-resolution data. In the whole energy range available in the decay, the predicted accumulated gross-theory strength is approximately a factor of two higher than the TAGS result, as can be seen from Fig. 15.

In Fig. 16 the comparison of the strength distribution deduced from the analysis with the high-resolution results and the predictions of gross theory is shown for the decay of

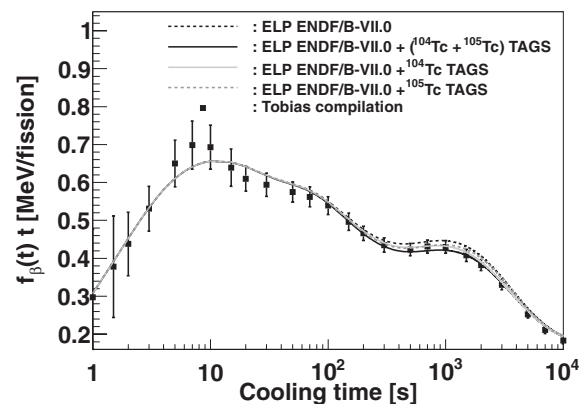


FIG. 11. Comparison of calculated  $\beta$  decay-heat component with data of Tobias compilation [23] after instantaneous fission event in  $^{239}\text{Pu}$ . The individual contributions of the  $^{104}\text{Tc}$  and  $^{105}\text{Tc}$  decays are also presented.

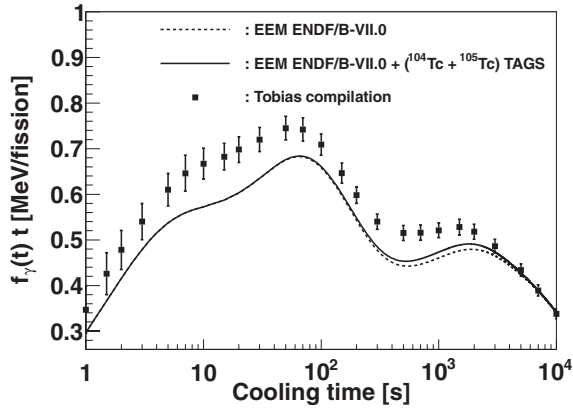


FIG. 12. Comparison of calculated  $\gamma$  decay-heat component with data of Tobias [23] after an instantaneous fission event in  $^{235}\text{U}$  without and with the inclusion of  $^{104}\text{Tc}$  and  $^{105}\text{Tc}$  TAGS measurements.

$^{105}\text{Tc}$ . The corresponding accumulated strength is presented in Fig. 17. Up to 1.7 MeV excitation energy, the TAGS results run below the high-resolution results and the gross theory predictions. Above this energy, TAGS strength increases, similar to the shape of the high-resolution strength distribution, which extends up to 2403.5 keV, the last populated level in high-resolution studies. For excitation energies higher than 2403.5 keV, the TAGS detects additional strength in agreement with the prediction of the gross theory. In the whole energy range available in the decay the TAGS accumulated strength value is approximately a factor of 0.8 lower than the gross theory prediction (see Fig. 17).

The  $\beta$ -strength distribution for the decay of  $^{102}\text{Tc}$  is shown in Fig. 18. If we sum the strength values in Fig. 18 up to the excitation energy of 2900 keV, which corresponds to the last known level from high-resolution measurements, we find that the integral value of the TAGS strength is higher than the integral value of high-resolution strength, and the gross theory prediction is one order of magnitude smaller. This can be seen directly from the accumulated strength values of Fig. 19 at the excitation energy of 2.9 MeV. In the whole energy interval ( $0 \leq E_{ex} < Q_{\beta}$ ) available in the decay the

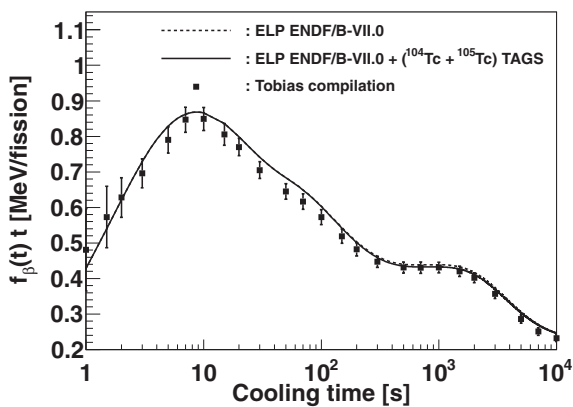


FIG. 13. Comparison of calculated  $\beta$  decay-heat component with data of Tobias compilation [23] after instantaneous fission event in  $^{235}\text{U}$ .

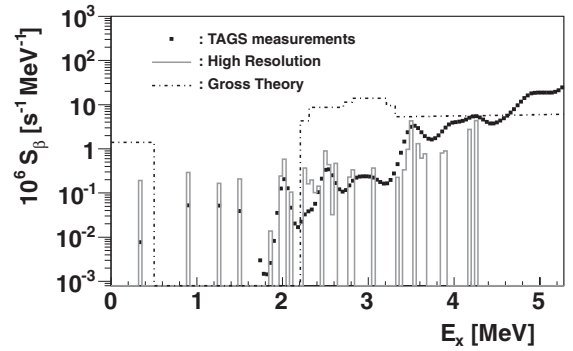


FIG. 14. Comparison of TAGS  $\beta$ -strength distribution for the decay of  $^{104}\text{Tc}$  with results from high-resolution measurements and calculations using gross theory.

gross theory predicts a strength value which is approximately four times less than the value measured with the TAGS. Gross theory fails to “generate” strength for the ground-state transition of  $^{102}\text{Tc}$ , which may not be surprising. In this model summations over the squared absolute value of the nuclear matrix elements are replaced by integrations of the function  $[|M_{\Omega}(E)|^2]$ . This function is deduced with the aid of sum rules for the strength function. Thus we can expect that global, smooth behavior of the strength function can be described with this model. The decay of  $^{102}\text{Tc}$  has a large amount of feeding concentrated in one level, which may not be easy to address with such a “gross” approach. This problem has been recognized and addressed recently in an attempt to define better the limitations of the application of the gross theory model in nuclear databases [26].

## V. EXCITED VAMPIR CALCULATIONS

The description of the Gamow-Teller (GT) strength distributions for the beta decay of neutron-rich nuclei in the  $A \sim 100$  region meets the difficulty of treating self-consistently the shape coexistence and mixing manifest in the structure of both odd-odd and even-even nuclei as well as the possible sudden onset of quadrupole deformation between neutron numbers  $N = 58$  and 60. It has also been suggested that triaxiality may also occur in this region of nuclei [6]. One model that may explain shape effects in this region is the complex excited VAMPIR variational approach.

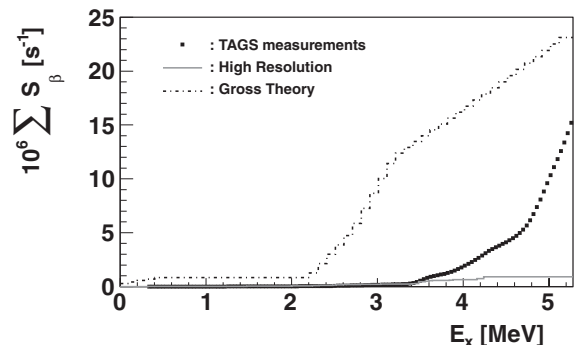


FIG. 15. Accumulated strength distributions for the decay of  $^{104}\text{Tc}$ .

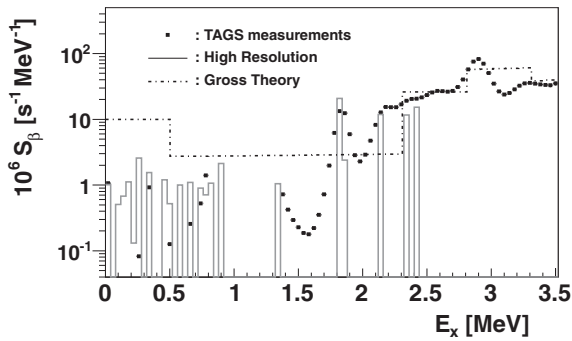


FIG. 16. Comparison of deduced  $\beta$ -strength distribution for  $^{105}\text{Tc}$  with high-resolution results and with predictions of gross theory.

Within this approach the low- and high-spin positive-parity states in an isotopic chain of even-mass neutron-rich zirconium isotopes have been studied. The calculations show an example of rapid transition from spherical to deformed shape [27]. In this framework the Gamow-Teller strength distributions,  $\beta$ -decay half-lives, and  $\beta$ -delayed neutron-emission probabilities for the  $^{104,106}\text{Zr}$  nuclei [28], and the triple shape coexistence and shape evolution in the  $N = 58$  Sr and Zr [29] isotopes have been described obtaining a rather good agreement with the available experimental data.

The VAMPIR approaches use Hartree-Fock-Bogoliubov (HFB) vacua as basic building blocks, which are only restricted by time-reversal and axial symmetry. The underlying HFB transformations are essentially *complex* and do mix proton with neutron states as well as states of different parity and angular momentum. The broken symmetries of these vacua (nucleon numbers, parity, total angular momentum) are restored by projection techniques and the resulting symmetry-projected configurations are used as test wave functions in chains of successive variational calculations to determine the underlying HFB transformations as well as the configuration mixing. The HFB vacua of the above type account for arbitrary two-nucleon correlations and thus include unnatural-parity correlations and simultaneously describe like-nucleon as well as isovector and isoscalar proton-neutron pairing. Furthermore, the complex excited VAMPIR model (EXVAM) allows the use of rather large model spaces and realistic effective interactions.

The present study is the first attempt to carry out a completely self-consistent calculation of the Gamow-Teller

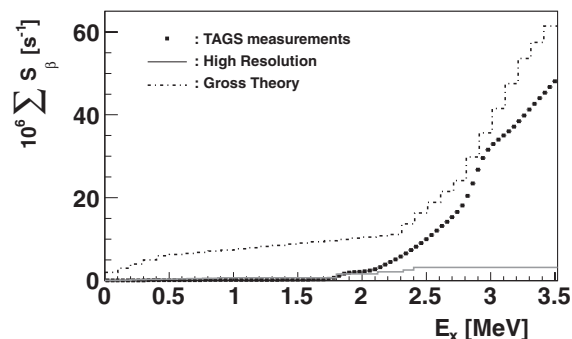


FIG. 17. Accumulated strength distributions for  $^{105}\text{Tc}$  decay.

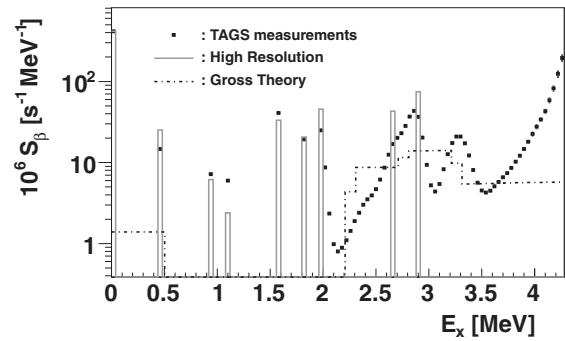


FIG. 18. Deduced  $\beta$ -strength distribution from the TAGS measurement for the  $\beta$ -decay of  $^{102}\text{Tc}$ . A comparison with high-resolution measurements and calculations using gross theory is also given.

$\beta$ -decay properties of the  $^{102}\text{Tc}$  and  $^{104}\text{Tc}$  nuclei. For nuclei in the  $A \simeq 100$  mass region we use a large model space above a  $^{40}\text{Ca}$  core built out of  $1p_{1/2}$ ,  $1p_{3/2}$ ,  $0f_{5/2}$ ,  $0f_{7/2}$ ,  $2s_{1/2}$ ,  $1d_{3/2}$ ,  $1d_{5/2}$ ,  $0g_{7/2}$ ,  $0g_{9/2}$ , and  $0h_{11/2}$  oscillator orbits for both protons and neutrons in the valence space. The effective two-body interaction is constructed from a nuclear matter  $G$  matrix based on the Bonn one-boson-exchange potential (Bonn A). This  $G$  matrix was modified by adding short-range (0.707 fm) Gaussians in the  $T = 1$  and  $T = 0$  channels in order to enhance the pairing correlations. In addition the isoscalar interaction was modified by monopole shifts for the  $T = 0$  matrix elements of the form  $\langle 0g_{9/2}0f; IT = 0 | \hat{G} | 0g_{9/2}0f; IT = 0 \rangle$  involving the  $0f_{5/2}$  and  $0f_{7/2}$  orbitals. The results reported here have been obtained using the effective Hamiltonian adjusted following a number of investigations of the neutron-rich nuclei in the  $A \simeq 100$  mass region [29]. We calculated the lowest  $1^+$  states in  $^{102}\text{Tc}$ , the lowest  $3^+$  states in  $^{104}\text{Tc}$ , and the positive-parity states up to spin  $4^+$  in  $^{102}\text{Ru}$  and  $^{104}\text{Ru}$ . For the description of the states involved in  $^{102}\text{Ru}$  we included in the excited VAMPIR many-nucleon basis up to 26 EXVAM configurations. The dimension of the many-nucleon EXVAM basis for the  $1^+$  states in  $^{102}\text{Tc}$  was 7. The calculations for the decay of  $^{104}\text{Tc}$  have been based on the same effective Hamiltonian. We used 25 EXVAM configurations for the calculated  $2^+$  and  $4^+$  states in  $^{104}\text{Ru}$  and 7 such projected configurations for the  $3^+$  parent state in  $^{104}\text{Tc}$ . The final solutions have been obtained by diagonalizing the residual interaction between the excited VAMPIR configurations for each spin. The results obtained indicate that the structure of

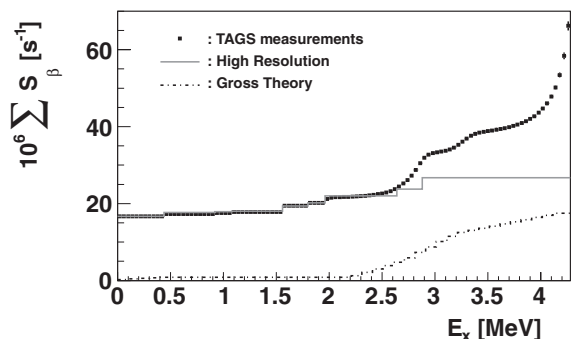


FIG. 19. Accumulated strength distributions for the decay of  $^{102}\text{Tc}$ .

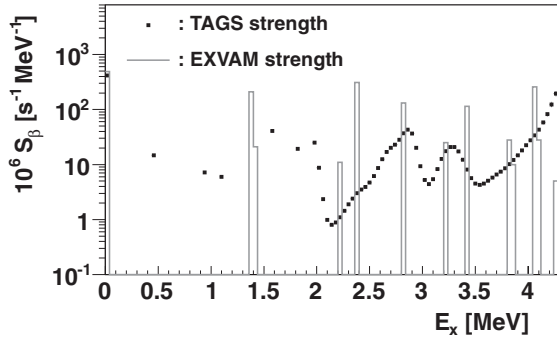


FIG. 20. Gamow-Teller strength distributions for the decay of  $^{102}\text{Tc}$  obtained within the complex excited VAMPIR calculations compared with TAGS strength results.

the wave function for the lowest  $1^+$  state of  $^{102}\text{Tc}$  manifests a strong mixing of differently deformed prolate and oblate configurations in the intrinsic system. Altogether the prolate components represent 53% of the total amplitude while the oblate components make up 47% of the structure of the wave function. The wave functions of the daughter states with significant Gamow-Teller strength manifest significant oblate-prolate mixing. The prolate mixing for the  $0^+$  states in  $^{102}\text{Ru}$  varies from 85% to 26%, while for the  $2^+$  states the prolate content varies from 78% to 26% of the total amplitude for the contributing states. In  $^{104}\text{Tc}$  the results indicate completely different structure properties. The  $3^+$  parent state is dominated by one prolate component which represents more than 99% of the total amplitude. The  $2^+$  and  $4^+$  daughter states in  $^{104}\text{Ru}$  manifest varying amounts of prolate-oblate mixing. For the states with significant GT strength the contribution of the prolate configurations to the structure of the  $2^+$  states varies from 82% to 9%, while the prolate mixing of the  $4^+$  states varies from 96% to 8%. The deformation of the states is larger in  $^{104}\text{Ru}$  with respect to  $^{102}\text{Ru}$ , as reflected in the spectroscopic quadrupole moments. The  $2^+$  states with significant Gamow-Teller strength contributions display quadrupole moments varying in  $^{102}\text{Ru}$  from  $-36.66 e \text{ fm}^2$  to  $30.07 e \text{ fm}^2$  (we used as effective charges  $e_p = 1.3$ ,  $e_n = 0.3$ ) while in  $^{104}\text{Ru}$  they vary from  $-43.99 e \text{ fm}^2$  to  $54.44 e \text{ fm}^2$ .

The Gamow-Teller strength distribution for the decay of the  $1^+$  parent state in  $^{102}\text{Tc}$  to the calculated  $0^+$  and  $2^+$  daughter

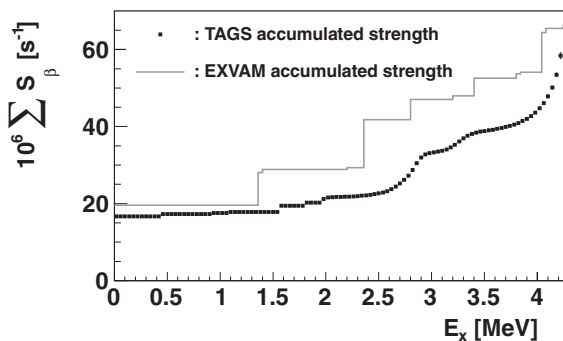


FIG. 21. Gamow-Teller accumulated strength distributions for the decay of  $^{102}\text{Tc}$  obtained within the complex excited VAMPIR calculations compared with TAGS strength results.

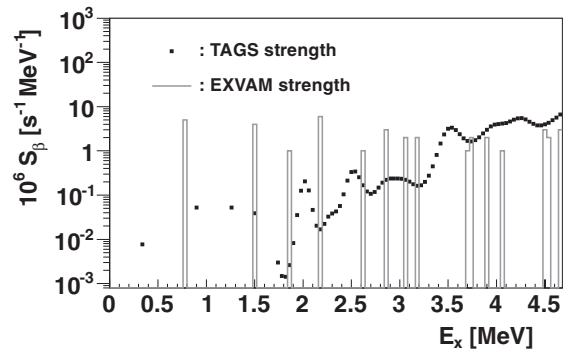


FIG. 22. Gamow-Teller strength distributions for the decay of  $^{104}\text{Tc}$  obtained within the complex excited VAMPIR compared with TAGS strength results.

states in  $^{102}\text{Ru}$  is presented in Fig. 20 compared with the TAGS results. The GT strength for the decay to the  $1^+$  states in  $^{102}\text{Ru}$  is negligible. The corresponding Gamow-Teller accumulated strength is compared with the TAGS results in Fig. 21. The obtained half-life for the decay of  $^{102}\text{Tc}$  into  $^{102}\text{Ru}$  within this approach is 6.6 s, to be compared with the experimental value of 5.3 (2) s, which shows a nice agreement.

The Gamow-Teller strength distribution for the decay of the  $3^+$  parent state in  $^{104}\text{Tc}$  to the calculated  $2^+$  and  $4^+$  daughter states in  $^{104}\text{Ru}$  (the  $3^+$  states do not have a significant contribution) is compared with the TAGS results in Fig. 22 and the GT accumulated strength in Fig. 23. In this case, the half-life is not so well reproduced. The obtained half-life within the excited VAMPIR approach is 385 s, to be compared with the experimental result of 1098 (18) s.

The strong Gamow-Teller  $\beta$ -decay branches indicate essential contributions from the  $g_{9/2}^\pi g_{7/2}^\nu$ ,  $d_{5/2}^\pi d_{3/2}^\nu$ , and  $d_{5/2}^\pi d_{5/2}^\nu$  matrix elements. Smaller contributions are obtained from the  $p_{1/2}^\pi p_{3/2}^\nu$  and  $p_{3/2}^\pi p_{1/2}^\nu$  matrix elements. In the decay of  $^{102}\text{Tc}$  to  $^{102}\text{Ru}$  the  $g_{9/2}^\pi g_{7/2}^\nu$  contribution is large and the  $d_{5/2}^\pi d_{3/2}^\nu$  is significant but smaller. The matrix elements  $d_{5/2}^\pi d_{5/2}^\nu$ ,  $p_{1/2}^\pi p_{3/2}^\nu$ , and  $p_{3/2}^\pi p_{1/2}^\nu$  show cancellations but they are significantly weaker. In the case of the decay of  $^{104}\text{Tc}$  to  $^{104}\text{Ru}$  the same matrix elements are relevant, but all of them are relatively small and the cancellations produce the final small strength for each Gamow-Teller contributing state. The strong mixing

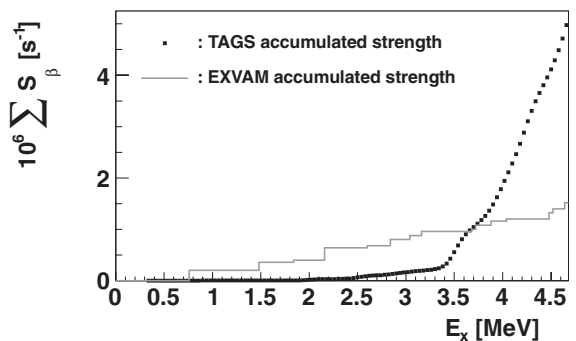


FIG. 23. Gamow-Teller accumulated strength distributions for the decay of  $^{104}\text{Tc}$  obtained within the complex excited VAMPIR compared with TAGS strength results.

of prolate and oblate projected configurations in the parent state as well as in the daughter states is responsible for the significant difference in the GT decays of  $^{102}\text{Tc}$  and  $^{104}\text{Tc}$ . Also the deformation of the main configurations in the structure of the wave functions is smaller in the first case where the number of neutrons in the daughter nucleus has the critical value  $N = 58$  [29] while in the second case the larger deformation is determined by  $N = 60$  in the  $^{104}\text{Ru}$  daughter nucleus.

## VI. CONCLUSIONS

In this article we have presented the detailed analysis of TAGS measurements for the decay of the  $^{102,104,105}\text{Tc}$  nuclei that were regarded as being important contributors to the decay heat in reactors. In the measurements three experimental techniques were combined for the first time to solve a long-standing problem in the description of the decay-heat data: IGISOL, to produce refractory elements, JYLTRAP, as a high-resolution isobaric separator, and the total-absorption technique. The results of our measurements

solve a large part of the discrepancy in the decay-heat data of  $^{239}\text{Pu}$  in the 300–3000 s cooling interval and show the importance of total-absorption measurements in addressing this problem. Nuclear structure calculations for the decay of  $^{102,104}\text{Tc}$  using the complex excited VAMPIR were also presented for the first time.

## ACKNOWLEDGMENTS

Discussions with Professor K. L. Kratz are acknowledged. This work was supported by the following projects: Spanish FPA 2005-03993, FPA2008-06419-C02-01, and FPA2011-24553; Hungarian OTKA K106035; Romanian CNCS-UEFISCDI project number PN-II-ID-PCE-2011-3-0153, German DFG FA67/36-1, the EC contract MERG-CT-2004-506849; the Finnish Center of Excellence Program 2006-2011 (Nuclear and Accelerator Based Physics Program at JYFL), and the the EU 6th Framework program (Integrating Infrastructure Initiative—Transnational Access), contract number: 506065 (EURONS).

- 
- [1] A. L. Nichols, FJ/OH Summer School 2000, Caradech, France, and references therein.
- [2] J. C. Hardy, L. C. Carraz, B. Jonson, and P. G. Hansen, *Phys. Lett. B* **71**, 307 (1977).
- [3] T. Yoshida *et al.*, *J. Nucl. Sci. Technol.* **36**, 135 (1999).
- [4] Assessment of Fission Product Decay Data for Decay Heat Calculation, Nuclear Science NEA/WPEC-25 (2007), Vol. 25.
- [5] A. Algora *et al.*, *Phys. Rev. Lett.* **105**, 202501 (2010).
- [6] P. Moller, R. Bengtsson, B. G. Carlsson, P. Olivius, and T. Ichikawa, *Phys. Rev. Lett.* **97**, 162502 (2006).
- [7] J. Äystö, *Nucl. Phys. A* **693**, 477 (2001).
- [8] V. Kolhinen *et al.*, *Nucl. Instrum. Meth. Phys. Res., Sect. A* **528**, 776 (2004).
- [9] A. Algora, ATOMKI Annual Report 2004, 17 (2005).
- [10] D. Cano-Ott *et al.*, *Nucl. Instrum. Methods Phys. Res., Sect. A* **430**, 488 (1999).
- [11] D. Cano-Ott *et al.*, *Nucl. Instrum. Methods Phys. Res., Sect. A* **430**, 333 (1999).
- [12] J. L. Tain and D. Cano-Ott, *Nucl. Instrum. Methods Phys. Res., Sect. A* **571**, 719 (2007).
- [13] J. L. Tain and D. Cano-Ott, *Nucl. Instrum. Methods Phys. Res., Sect. A* **571**, 728 (2007).
- [14] The GEANT4 program package; S. Agostinelli *et al.*, *Nucl. Instrum. Methods Phys. Res., Sect. A* **506**, 250 (2003).
- [15] <http://www-nds.iaea.org/ripl/>.
- [16] J. Blanchot, *Nucl. Data Sheets* **108**, 2035 (2007).
- [17] P. Möller and J. R. Nix, *At. Data Nucl. Data Tables* **59**, 185 (1995).
- [18] D. De Frenne and E. Jacobs, *Nucl. Data Sheets* **105**, 775 (2005).
- [19] D. De Frenne and E. Jacobs, *Nucl. Data Sheets* **83**, 535 (1998).
- [20] M. B. Chadwick *et al.*, *Nucl. Data Sheets* **107**, 2931 (2006).
- [21] Joint Evaluated Fission and Fusion File, Incident-neutron data, <http://www-nds.iaea.org/exfor/endl00.htm>, 2 October 2006; see also A. Koning, R. Forrest, M. Kellett, R. Mills, H. Henriksson, Y. Rugama, The JEFF-3.1 Nuclear Data Library, JEFF Report 21 (OECD/NEA, Paris, 2006).
- [22] A. Sonzogni (private communication).
- [23] A. Tobias, *Prog. Nucl. Energy* **5**, 1 (1980); Derivation of decay heat benchmarks for  $^{235}\text{U}$  and  $^{239}\text{Pu}$  by a least squares fit to measured data, RD/B/6210/R89 (1989).
- [24] K. Takahashi and M. Yamada, *Prog. Theor. Phys.* **41**, 1470 (1969).
- [25] K. Takahashi, *Prog. Theor. Phys.* **45**, 1466 (1971).
- [26] N. Hagura, T. Tachibana, and T. Yoshida, *J. Nucl. Sci. Technol.* **47**, 492 (2010).
- [27] A. Petrovici, K. W. Schmid, and A. Faessler, *J. Phys.: Conf. Ser.* **312**, 092051 (2011).
- [28] A. Petrovici, K. W. Schmid, and A. Faessler, *Prog. Part. Nucl. Phys.* **66**, 287 (2011).
- [29] A. Petrovici, *Phys. Rev. C* **85**, 034337 (2012).